Welding International

ISSN: 0950-7116 (Print) 1754-2138 (Online) Journal homepage: http://www.tandfonline.com/loi/twld20

Effect of welding parameters on microstructure of Fe-based nanostructured weld overlay deposited through FCAW-S

Agustín Gualco, Hernán G. Svoboda & Estela S. Surian

To cite this article: Agustín Gualco, Hernán G. Svoboda & Estela S. Surian (2016): Effect of welding parameters on microstructure of Fe-based nanostructured weld overlay deposited through FCAW-S, Welding International, DOI: 10.1080/09507116.2015.1096533

To link to this article: http://dx.doi.org/10.1080/09507116.2015.1096533

WELDING INTERNATIONAL, 2016
http://dx.doi.org/10.1080/09507116.2015.1096533

Taylor & Francis
Taylor & Francis Group

Effect of welding parameters on microstructure of Fe-based nanostructured weld overlay deposited through FCAW-S

Agustín Gualco[a], Hernán G. Svoboda[b,c] and Estela S. Surian[a]

[a]Faculty of Engineering, Secretariat of Research, National University of Lomas de Zamora, Buenos Aires, Argentina; [b]Faculty of Engineering, Laboratory of Materials and Structures and Department of Mechanical Engineering, Laboratory of Material and Structures, University of Buenos Aires, INTECIN, Argentina; [c]National Scientific and Technical Research Council, Argentina

ABSTRACT

Lately, modern hardfacing tubular wires for semiautomatic welding with gas protection and without it have been developed. These wires deposit Fe-based nanostructured alloys with high abrasive wear resistance. The information on these new consumables is scarce, especially about the effect that the welding parameters (heat input, shielding gas, arc voltage, current intensity, etc.) have on the deposit, its microstructure and, consequently, its wear behaviour. For this reason, in this article, we study the effect of heat input (voltage, intensity of current and welding velocity) on the properties of a flux-cored arc welding Fe-based nanostructured deposit obtained without gas protection. This study is a continuation of a previous one in which the same consumable was used under shielding gas. Bead on plate samples were welded using heat inputs between 0.5 and 3.5 k/mm. The dimensional study was performed on the beads, chemical composition was determined and the microstructure was analysed using optical and electronic microscopy and X-ray diffraction. Microhardness, crystallite size and dilution percentage were also measured. An important influence of the welding parameters on the bead geometry and the microstructure was observed. The operational behaviour of this wire, welded without shielding gas, was very good.

KEYWORDS

Hardfacing deposits; open arc wire; nanomaterials; heat input; microstructure

1. Introduction

The flux-cored arc welding (FCAW) process is one of the most commonly used processes for overlaying new pieces or repairing used ones. It is possible to deposit layers with high efficiency from a few to a few tens of kilos of metal welding deposit per hour [1,2].

In the past few years, there has been great interest in the production of self-shielded flux-cored wires which deposit iron alloys with a matrix of nanostructured α-ferrite with precipitated carbides and borides [3–5], which provides the deposits with high resistance to abrasive and erosive wear. From recent studies and due to the sensitivity of these wires to the operative parameters, it was decided to further examine the behaviour of these new consumables and to study the influence of the thermal input on the bead geometry, the dilution, the microstructure, the size of the crystallite and the microhardness of the nanostructured Fe-based alloy deposits, obtained using a flux-cored wire by means of semiautomatic welding without shielding gas. This article is a continuation of another which has already been published [6], in which the same consumable is studied, welded using the same process, but with Ar-20%CO_2 shielding gas.

2. Materials and methods

2.1. Consumable used

The consumable used was a commercial flux-cored wire of 1.6 mm diameter, deposited by means of the semi-automatic welding process without shielding gas, in a mechanised form, using a Miggytrac device.

2.2. Welding of the pure weld coupon

In order to determine the chemical composition of the undiluted deposit, a pure weld coupon is welded for chemical analysis (Figure 1). The sequence of the same was 3 layers with 4, 3 and 2 beads in the flat position. The welding parameters used were 300 A, 35 V and 5 mm/s of forward speed.

2.3. Welding of the test pieces to study the heat input (HI)

Eight coupons were welded in the flat position, each with one bead, on base plates of 150 × 75 × 12.5 mm made from carbon steel type SAE 1010, as is shown schematically in Figure 2. The welding parameters used can be seen in Table 1, as well as the identification used and the

Selected from *Soldagem & Inspeção* 19(3) 255–263.

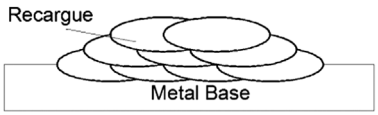

Figure 1. Outline of the pure weld coupon. Recargue = Overlay; Metal Base = Base Metal.

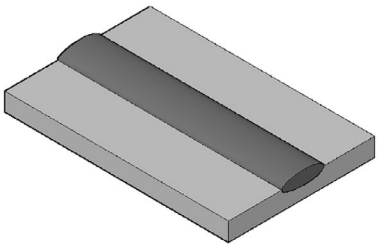

Figure 2. Outline of the test piece with a single bead.

heat input in each case. The free length of the wire was 25 mm in all cases. The different test pieces were grouped into two series referred to with the letters L (low) and H (high), associated with the electrical power used; the number added to the letter corresponds to the welding speed used.

In accordance with the chosen welding parameters, two pairs of test pieces were welded with different power and welding speed, but with similar or equal heat input. These test pieces are H7 and L3 with 1.5 and 1.7 kJ/mm of heat input, respectively, and, on the other hand, H10 and L5, both with 1.0 kJ/mm.

After the welding of the different test pieces, a visual inspection was implemented to detect the presence of superficial macroscopic defects.

2.4. Chemical, macro- and microstructural characterisations of the HI test pieces

Chemical composition measurements were carried out over the cross sections by means of energy dispersive X-ray spectroscopy. The dimensions of the beads – thickness, penetration and height – were measured by means of image analysis software. The microstructure was characterised by means of scanning electron microscopy (SEM).

X-ray diffraction (XRD) was carried out over the surface of each bead. The equipment used was a RIGAKU, with Cu K-α radiation, between 35 and 95°, with a scanning speed of 1°/min. From the spectra obtained, the present phases were analysed and the crystallite of the α-ferrite phase was determined using the Scherrer formula [7,8].

2.5. Study of dilution of the HI test pieces

The percentage dilution was calculated from the areal relations between the melted metal and the base metal. The measurements were implemented by means of image analysis software. Dilution estimates were also conducted by means of variations of the % Cr between the base plate and the pure weld metal.

2.6. Study of hardness over the HI test pieces

The Vickers microhardness (HV2) was measured at 1 mm from the surface over five zones of the cross sections, providing the values obtained. The microhardness over the phases was also determined with HV0.05.

3. Results and discussion

3.1. Chemical composition of the pure weld metal

In Table 2, the result of the chemical analysis obtained from the test piece of pure weld metal is shown.

The deposited material presented a high concentration of alloying elements within the Fe-(Nb,Cr)-(C,B) system. The chemical composition fulfils the regulations for the formation of nanostructures, which are (a) that the system has multiple components with at least three alloying elements; (b) a difference of atomic radius between the elements which constitute the alloy system of more than 12% and (c) that the heat of the mixture between its three main elements is negative [9,10]. These characteristics produce great difficulties for the

Table 1. Welding parameters.

Identification	Arc voltage (V)	Current intensity (A)	Electrical power (kW)	Welding speed (mm/s)	Heat input (kJ/mm)
L3	25	200	5.0	3	1.7
L5	25	200	5.0	5	1.0
L7	25	200	5.0	7	0.7
L10	25	200	5.0	10	0.5
H3	35	300	10.5	3	3.5
H5	35	300	10.5	5	2.1
H7	35	300	10.5	7	1.5
H10	35	300	10.5	10	1.0

Note: L: low electrical power H: high electrical power.

Table 2. Chemical composition of the pure weld metal (% by weight).

C	Mn	Si	Cr	Nb	B	Fe
0.99	0.22	1.02	16.8	4.6	4.6	Balance

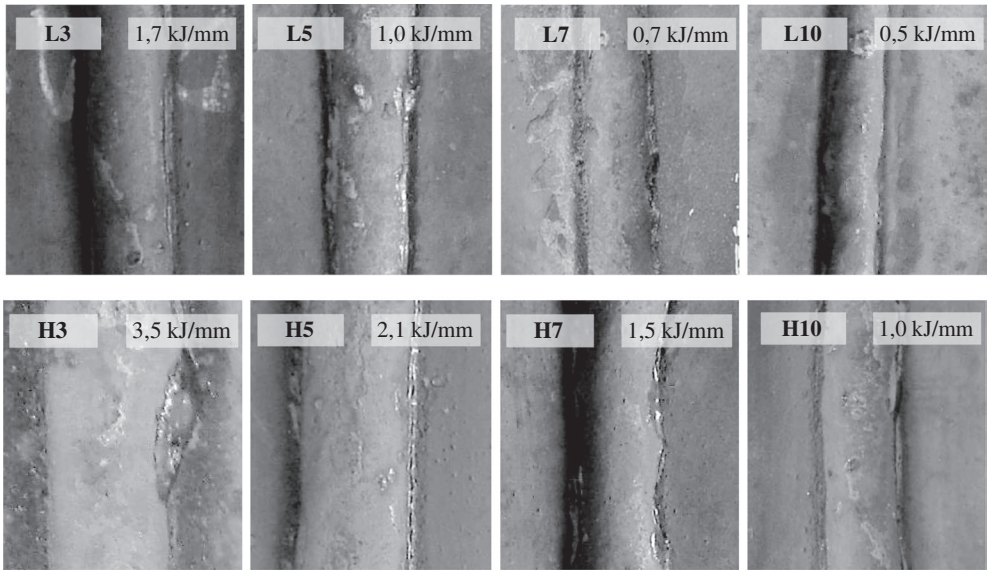

Figure 3. Top view of the welded joints (1×).

nucleation and the growth of layers of regular atoms, producing crystals of nanometric size.

3.2. Analysis of the HI test pieces

3.2.1. Visual inspection

The photographs acquired of the different welded beads are shown in Figure 3.

Slag was found on the sides of the beads. The cases of spatter were few and small in size. The surface finish was good, and beach marks were not observed. Transversal fissures were produced at the bead, produced by the relief of tension typical in these materials.

3.2.2. Macrograph and dimensional analysis of the beads

Macroscopic defects such as pores or inclusions were not observed: Figure 4. Good adherence of the beads was observed and there was good wetting.

It was observed that the shape of the fusion line in the welded test pieces (L3, H3, L5 and H5) was in the shape of a 'mushroom'.

The measured values for thickness, penetration and height of each one of the beads is presented in Table 3.

In Figure 5, the changes of thickness, penetration and height of the bead are presented as a graph with the welding speed, the L and H series depicted separately, in order to see the effect of the power used.

As a general tendency, an increase in welding speed (or decrease in heat input) produced a reduction in the values for bead thickness (from 16 to 8 mm), penetration (from 3 to 1.8 mm) and height (from 4 to 2 mm). The increase in the electrical power used generated increases in the bead thickness and the height, but did not seem to have an important influence on the penetration. This is consistent with what is reported in the bibliography [2]. The test pieces with similar heat input presented variations in the bead geometry, mainly in the thickness. This was explained by the increase in arc voltage, which tends to flatten the bead, and the greater deposition with the increase in current [2].

It is interesting to note that when the electrical power increases (for the same values of heat input), greater height and thickness and less variation in penetration is observed, all desirable characteristics for the overlay.

3.2.3. Dilution studies

The results of the dilution calculations [2], carried out based on the macro photographs of the cross sections, are presented in Table 4.

The percentage dilution varied between 25 and 38% for the different welding conditions. It was observed that the lower values of dilution were present in the welded test pieces with high heat input. This was associated with the greater input of material which is produced during welding without shielding gas with the increase of the electrical power and with the shape of the fusion line which generates a low level of mixing with the base metal (Figure 4).

The results obtained for the values of Cr are presented in Table 5.

It was observed that when the thermal input increased, there was a greater concentration of Cr. This could be explained by the lesser dilution due to the greater input of material and a low penetration [2]. Large differences with respect to the speed variation were not observed.

The average dilution values were calculated for each test piece from the data obtained for the metal composition of the pure weld metal and of the base material for each bead. In Figure 6, the results obtained are shown together with the determined dilution values in Table 3.

Differences of less than 10% were observed between the dilution measured over the macros and the calculations carried out considering the chemical composition.

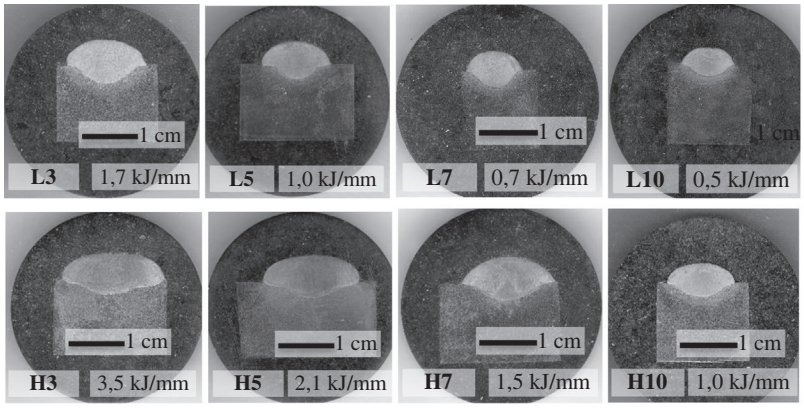

Figure 4. Macrostructure of the welded test pieces without shielding gas.

Table 3. Thickness, penetration and height measured over the different deposited beads.

Test piece	L3	L5	L7	L10	H3	H5	H7	H10
Heat input (kJ/mm)	1.7	1.0	0.7	0.5	3.5	2.1	1.5	1.0
Forward speed (mm/s)	3	5	7	10	3	5	7	10
Bead thickness (mm)	12.4	11.0	8.4	8.0	16.6	15.5	14.6	10.3
Penetration (mm)	3.0	2.5	2.3	1.8	2.8	2.5	2.4	2.1
Height (mm)	3.8	3.6	3.4	2.7	4.2	4.2	4.1	3.4

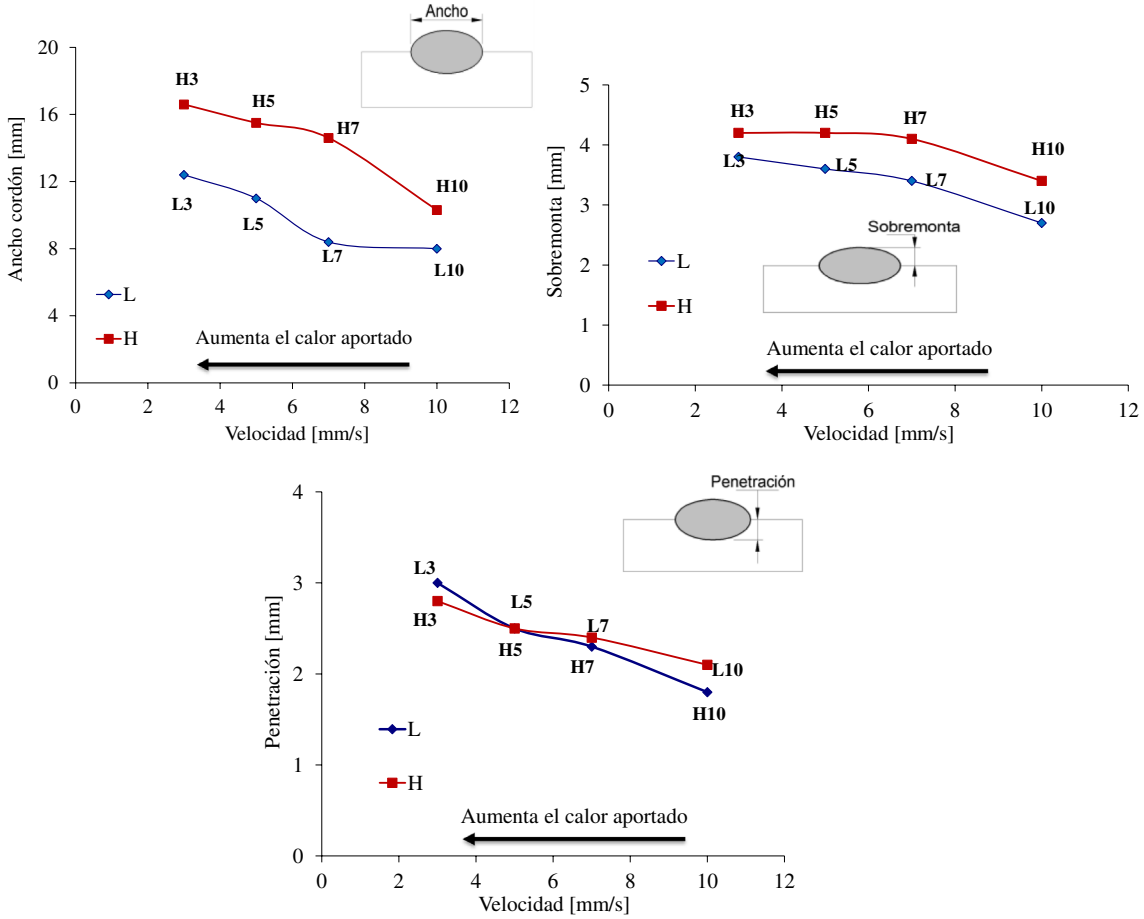

Figure 5. Bead thickness, height and penetration versus welding speed. Ancho cordon = Bead thickness; Aumenta el calor aportado = Increase in heat input; Ancho = Thickness; Velocidad = Speed; Sobremonta = Height; Penetración = Penetration.

This was associated with the oxidation produced during the reactions in the molten pool.

In contrast with what was reported in the previous paper [6], from which this is a continuation and in which welding takes place using Ar-20%CO_2 gas, it can be seen that when the heat input was increased, the dilution decreased. This is consistent with that which is observed in the graphs depicting penetration, thickness

Table 4. Dilution for the different welding conditions.

Test piece	L3	L5	L7	L10	H3	H5	H7	H10
Heat input (kJ/mm)	1.7	1.0	0.7	0.5	3.5	2.1	1.5	1.0
Dilution (%)	32	28	37	38	28	25	32	33

Table 5. Cr concentration in the different deposited beads (% by weight).

Test piece	L3	L5	L7	L10	H3	H5	H7	H10
Heat input (kJ/mm)	1.7	1.0	0.7	0.5	3.5	2.1	1.5	1.0
Cr	10.2	10.9	9.8	10.3	12.4	12.7	11.5	11.6

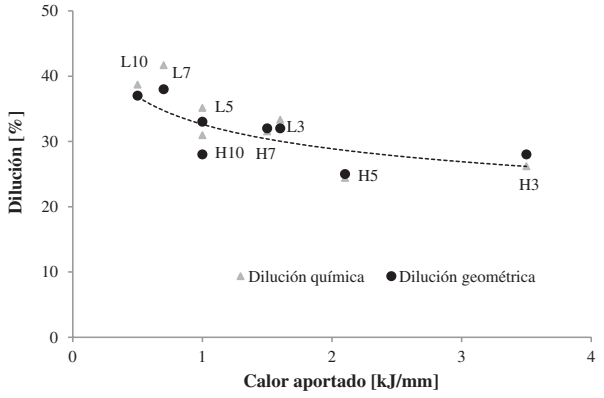

Figure 6. The relationship between the chemical and geometric dilutions and the heat input of all beads. Dilución = Dilution; Dilución química = Chemical dilution; Dilución geométrica = Geometric dilution; Calor aportado = Heat input.

and height and in the macro cuts. This is the ideal condition: maximum input and low dilution are obtained.

3.2.4. Microstructural characterisation

XRD spectra were implemented over the surface of all samples, Figure 7.

It can be seen that the structure was formed mainly by α-Fe, metallic carboborides ($M_7(BC)_3$, $M_{23}(BC)_6$) and niobium carbides (NbC). Variations of the present phases were observed with the thermal input for the welded test pieces with high heat input H3 and H5 (less dilution) which showed greater presence of $M_{23}C_6$. This was related to the greater content of alloying elements as a product of the lower dilution which was obtained in these final test pieces. The size of the crystallite was 105 and 125 nm, variations which could be related to the total percentage of alloying elements in the matrix [11,12], which could affect the formation of the nanocrystals.

The SEM images of the microstructures are shown in Figure 8.

In Figure 8(a) and (b) (L3 and L10), a pattern of dendritic segregation can be observed where the values of Cr were 12% in the interdendritic zone and 7% within the dendritic region, indications A and B in Figure 8(d) respectively. Said pattern becomes finer as the thermal input decreases. A laminar/globular structure (M_7X_3) can be seen in the interdendritic zone, which also becomes finer as the thermal input decreases.

Figure 8(c) shows the presence of $M_{23}(CB)_6$ and NbC.

Two solidification patterns were observed as a function of the heat input and the dilution.

In the first pattern, the α-Fe phase is formed and then the eutectic system is precipitated in the interdendritic zone, comprised of flat and globular layers of precipitates of type M_7X_3 and α-Fe (Figure 9(a) and (b)). In the second pattern, found in the samples with low dilution (H3 and H5), initially the NbC precipitates, and then the carboboride complexes $M_{23}X_6$ nucleate over them with the decrease in temperature, as is indicated in Figure 9(c); finally, the eutectic system, M_7X_3 and α-Fe [13–15] form from the remaining liquid, Figure 9(d). This mode of solidification was found in recent papers [16,17] with the consumable being studied, carried out in 1 and 2 layers, where the dilution was lower.

3.2.5. Microhardness

In Table 6, the results of the measured microhardness are observed, presented as an average of at least three measurements.

It can be seen that the values vary between 825 and 882 HV2, being consistent with that which is expected for this material [15,18,19]. The tests pieces with similar thermal input presented variations in the hardness despite having almost the same dilution, which was related to the present phases and their microhardness.

It was observed that the microhardness of the eutectic phase increased with the increase in the welding speed. This was associated with a refinement of said phase which produced a greater restriction of the movement of the dislocations and as a consequence greater hardness [20]. A decrease in the fraction of the α-Fe phase was also observed with the increase in the heat input (L5 has a greater fraction of α-Fe than H5 and is greater than H3), Figure 10(a)–(c), and a globular/laminar eutectic system which is thicker and has a lower microhardness (925, 837, 822 Hv for L5, H5 and H3, respectively). This phenomenon was explained by the lower level of dilution, Figure 6, which favours the second mode of solidification. The presence of carboborides $M_{23}X_6$ of high hardness was also observed which probably had a low incidence in the macro hardness due to its low fraction in volume, evaluated visually.

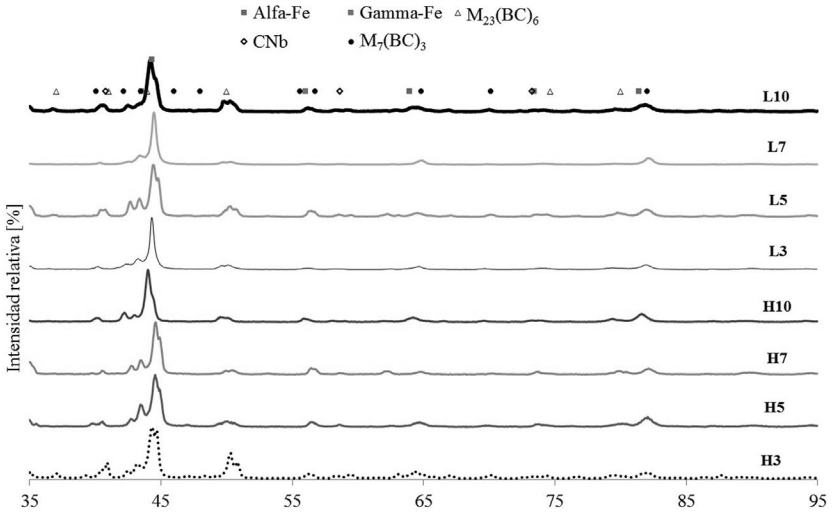

Figure 7. XRD spectra of all conditions. Intensidad relative = Relative intensity.

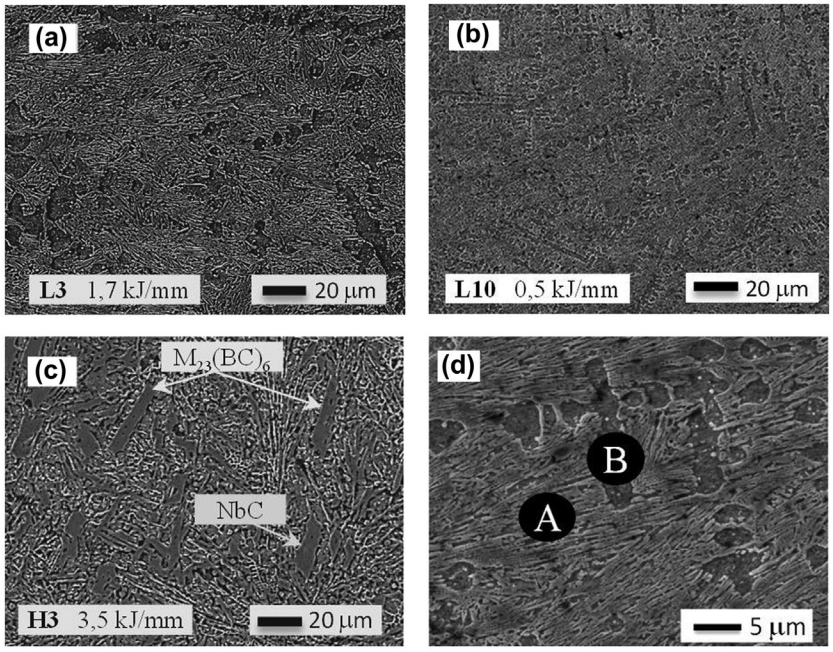

Figure 8. SEM micrographs of the test pieces L10, L3 and H3.

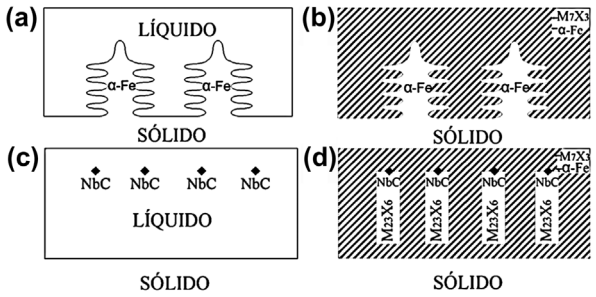

Figure 9. Modes of solidification. LÍQUIDO = liquid; SÓLIDO = solid.

4. Conclusions

In this study, the effect of the welding parameters on the characteristics of the deposits of Fe-based nanostructured alloy, obtained using the FCAW process without shielding gas, with thermal inputs between 0.5 and 3.5 kJ/mm, was evaluated.

It was concluded that:

- All the test pieces welded presented a good surface finish and low levels of spattering and of slag. The majority cracked during cooling.
- A decrease in the values of the bead thickness, penetration and height was produced at a greater welding speed (or decrease of the heat input). The increase in the electrical power used generated increases in the bead thickness and height, but did not seem to have an important influence on the penetration. The test pieces welded with similar heat input presented variations in the geometry of the beads, mainly in the thickness.

Table 6. Microhardness [HV2].

Test piece	L3	L5	L7	L10	H3	H5	H7	H10
Heat input (kJ/mm)	1.7	1.0	0.7	0.5	3.5	2.1	1.5	1.0
Dilution (%)	32	28	37	38	28	25	32	33
Hardness	867	882	871	856	833	837	829	825

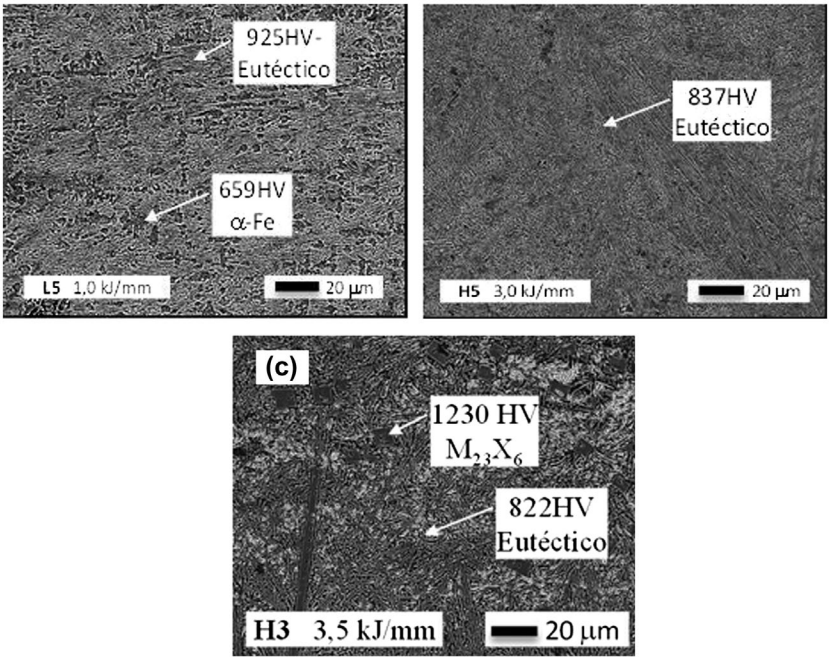

Figure 10. Microhardness values of the phases of the test pieces L5, H5 and H3. Eutectic system: α-Fe + $M_7(BC)_3$. Eutéctico = Eutectic system.

- The deposited material presented a dilution of 25–28% for the welded test pieces with the greatest thermal inputs and 33–38% for those welded with less thermal input.
- The microstructure was formed by a matrix of α-Fe, carboborides ($M_7(BC)_3$, $M_{23}(BC)_6$) and NbC. Variations were observed in the present phases with the thermal input; H3 and H5 (less dilution) showed a greater presence of $M_{23}C_6$. The size of the crystallite varied between 105 and 125 nm. A finer pattern of dendritic segregation was observed with lower thermal input. In the interdendritic zone, a laminar/globular structure was seen with the same behaviour. It was observed that the two-phase fraction increased when the heat input increased.
- The hardness varied with the thermal input from 825 to 882 HV. The test pieces with similar thermal input presented variations in hardness despite having almost the same dilution. It was observed that the microhardness of the eutectic phase increased with the increase in the welding velocity. A decrease in the fraction of the α-Fe phase was also observed with the increase in the heat input, and a thicker globular/laminar eutectic system of lower microhardness. The presence of carboborides $M_{23}X_6$ of high hardness was detected.
- In conclusion, the presented results showed that it is possible to weld with high heat input, obtaining low dilution of the overlay material, which suits the second mode of solidification which generates a greater proportion of the hard carbides, which is desirable in these applications.

Acknowledgements

The authors would like to thank EUTECTIC-CONACRO Argentina for the provision of the consumable used, AIR LIQUIDE Argentina for the donation of the welding gases, EUTECTIC-USA for the implementation of the chemical analyses, LABORATORIO DE MICROSCOPÍA ELECTRÓNICA DE INTI – MECÁNICA for the implementation of the scanning electron microscopy and APUENFI (Association of Entrepreneurial Professors in the Mechanical Field of the Faculty of Engineering – National University of Lomas de Zamora) for its economic support in the present project.

Disclosure statement

No potential conflict of interest was reported by the authors.

References

[1] Linnert GE. Welding metallurgy of carbon and alloy steels. 4th ed. Miami, FL: AWS; 1994. 474 p.
[2] Merrick S, Kotecki D, Wu J. Materials and applications – part 2. Welding Handbook. American Welding Society; 1998.

[3] Heath G. Nanotechnology and welding – actual and possible future applications. Proceedings of the Castolin-Eutectic Seminar, Brussels, Belgium; 2006. p. 25–35.
[4] Allen S, Edwin T. The structure of materials. New York (NY): Wiley; 1999.
[5] Klimpel A, Janicki D. A study of worn wear plates of fan blades of steel mill fumes suction system. Proceedings of the 13th Scientific International Conference, "Achievements in Mechanical and Materials Engineering" AMME'2005, Polonia, Gliwice; 2005. p. 307–310.
[6] Gualco A, Svoboda HG, Surian ES. Efecto de los parámetros de soldadura sobre la microestructura de recargues nanoestructurados base hierro. In: Gualco A, Svoboda HG, Surian E, editor. Soldagen & Inspecao. Vol. 18; 2013.
[7] Cullity BD, Stock SR. Elements of X-ray diffraction. 3rd ed. Prentice Hall; 2001. 520 p.
[8] Xpowder diffraction spectra analysis software, 2004 version.
[9] Datasheet: TeroMatec 395NOA. Eutectic Castolin-ESAB; 2008.
[10] Gleiter H. Nanostructured materials: basic concepts and microstructure. Acta Mater. 2000;48:1–29.
[11] Weissmüller J. Alloy effects in nanostructures. Nanostruct. Mater. 1993;3:261–272.
[12] Inoe A. Amorphous and nanocrystalline materials: preparation, properties, and applications. Springer; 2010. p. 206.
[13] Zhi X, Xing J, Fu H. Effect of niobium on the as-cast microstructure of hypereutectic high chromium cast iron. Mater. Lett. 2008;62:857–860.
[14] Ma S, Xing J, Liu G, Yi D. Effect of chromium concentration on microstructure and properties of Fe–3.5B alloy. Mater. Sci. Eng. A 2010;527:6800–6808.
[15] Branagan DJ, Marshall MC, Meacham BE. High toughness high hardness iron based PTAW weld materials. Mater. Sci. Eng. A 2006;428:116–123.
[16] Gualco A, Svoboda HG, Surian ES. Efecto del número de capas de soldadura sobre la resistencia al desgaste de recargues nanoestructurados base Fe, soldados con protección gaseosa y sin ella. Sao Paulo: XL Consolda; 2014 Oct 20–23.
[17] Gualco A, Marini C, Svoboda HG, Surian ES. Efecto del tratamiento térmico post-soldadura sobre la resistencia al desgaste de recargues nanoestructurados base hierro. Santa Fe (NM): SAM/CONAMET; 2014 Oct 20–23.
[18] Weissmüller J. Some basic notions on nanostructured solids. Mater. Sci. Eng. A 1994;179–180:102–107.
[19] Morris DG. The origins of strengthening in nanostructured metals and alloys. Revista de Metalurgia. 2010;46:173–186.
[20] Verhoeven JD. Fundamentos de la Metalúrgia Física. Ed Limusa, 1st version; 1987.